Mantle Values of Thermal Conductivity and the Geotherm from Phonon Lifetimes

A. M. Hofmeister

A model for thermal conductivity κ, based on phonon lifetimes obtained from infrared reflectivity, replicates experimental data at ambient conditions. The pressure and absolute temperature dependences of transport properties are accurately obtained from the Grüneisen parameter γ_{Th}, bulk modulus K_T, and thermal expansivity α: The lattice contribution κ_{lat} equals $\kappa_{298}(298/T)^a \exp[-(4\gamma_{Th} + 1/3) \int_{298}^{T}\alpha(\theta)d\theta]$ with $a = 0.33$ for silicates (or 0.9 for MgO), and $\partial[\ln(\kappa_{lat})]/\partial P = (1/3 + 4\gamma_{Th})/K_T$. The smaller, pressure-independent radiative contribution κ_{rad} equals $0.0175 - 0.0001037T + (2.245T^2/10^7) - (3.407T^3/10^{11})$, in units of watts per meter-kelvin, if Fe^{2+} is present. The resulting lithospheric geotherm is steep. Consequently, the mantle geotherm is hot if the low-velocity zone is anhydrous, but cold if hydrated.

An understanding of planetary heat transport requires knowledge of thermal conductivity (κ) and thermal diffusivity [$D = \kappa/(\rho C_P)$, where ρ is density and C_P is heat capacity at constant pressure] as functions of pressure (P) and absolute temperature (T). Conduction for steady-state flow along the Z direction in an isotropic medium is described by Fourier's law:

$$Q = -\kappa(\partial T/\partial Z) \qquad (1)$$

where Q is the heat flux (*1*).

For hard solids, conventional measurements of κ—that is, those involving physical contact—are problematic even at ambient conditions, and experimental discrepancies commonly exceed 20% (*2*). Measurements at high T are complicated by fugacity problems and radiative effects. For example, at 1200 K for (001) faces of olivine (with 90% Mg) crystals, κ ranges from 3.0 to 5.6 W/(m·K) (*3, 4*). Problems are compounded during compression because deformation produces uncertainties in the geometrical parameters used to solve Eq. 1 and cracking reduces thermal contact (*2, 5*). Discrepancies among pressure derivatives attain 1000%. A new technique, picosecond transient grating spectroscopy (PTGS), circumvents these problems and provides D up to ~10 GPa (*6–8*). However, few samples have been examined, such measurements at elevated temperature are under development (*9*), and sample size requirements limit pressures to ~40 GPa (*6–8*). Thus a theory, as I present here, is needed to extrapolate scant existing data to mantle conditions.

Heat transport can be related to microscopic behavior. In a semi-classical picture of the insulator, input of heat excites vibrations of the nearby atoms. Because atoms are connected by chemical bonds, the vibrational energy is dissipated through excitation of vibrations of adjacent atoms. A more realistic model accounts for quantization of these lattice vibrations, called phonons. Heat is thus transferred through phonons colliding with each other and possibly with defects or grain boundaries. Because raising pressure (or lowering temperature) raises vibrational frequencies and densification increases the chances of collision, κ increases as P increases (or as T decreases). If the energy is transferred randomly in local equilibrium [for example, (*10*)], then the contribution of phonon scattering to thermal conductivity is derived by analogy to the kinetic theory of gases (*11*):

$$\kappa_{lat} = \frac{1}{3}\sum_{j=1}^{3}\sum_{i=1}^{3p} c_{ij}u_{ij}^2\tau_i \qquad (2)$$

where $c_{ij} = x_{ij}^2 \exp(x_{ij})/[1 - \exp(x_{ij})]^2$ is the Einstein heat capacity per volume of the ith vibrational mode, $x_{ij} = h\omega_i(\mathbf{q}_j)/kT$, h is Planck's constant, k is Boltzmann's constant, $u_{ij} = d\omega_i/d\mathbf{q}_j$ is the group velocity, $\mathbf{q}_j$ is the wave vector, ω_i is the mode frequency, τ_i is the mean free lifetime between scattering events, $i = 1p$ to $3p$ sums the normal modes of a crystal with p atoms, and $j = 1$ to 3 sums the three orthogonal directions (*12*).

All previous calculations used only acoustic modes in Eq. 2, and moreover estimated τ_i (for example, *2, 6–8, 13–15*). Such models are of limited utility. For example, the use of an Einstein model for the acoustic modes underestimated κ_{lat} at ambient conditions for seven different solid solutions by 28 to 57% (*16*), whereas the measured pressure dependence of D for olivine (*7*) is larger than that predicted (*17*) by 50 to 100%, depending on the particular assumption used for τ_i.

In addition to transport by conduction, a hot material produces blackbody radiation, which travels as an electromagnetic wave. Heat is diffused if the light emitted by one particle is partially scattered or partially absorbed by high-frequency transitions in neighboring particles:

$$\kappa_{rad} = \frac{4\pi}{3}\int_{0}^{\infty} \lambda(\omega,T)\frac{\partial I(\omega,T)}{\partial\omega}d\omega \qquad (3)$$

where $\lambda(\omega,T) = u\tau$ is the mean free path and I is the intensity of the blackbody radiation (*20, 21*). Local equilibrium and optically thick conditions are assumed. Because this process occurs simultaneously with collisions of lattice phonons, the total conductivity κ of Eq. 1 is the sum of κ_{lat} and κ_{rad}. A laser heating technique has been used to measure κ_{rad} for a few minerals (*18, 19*). Other determinations involve calculations from spectroscopic measurements (*20, 21*). Previously, $1/\lambda$ was approximated by the absorption coefficient A (*20–23*). Typically, uniform extinction is further assumed and A is an average over visible or near-infrared (IR) regions, or both (*2, 22*). Shankland *et al.* (*23*) included the wavelength dependence of A obtained from visible and near-IR spectra of olivine in Eq. 3. Their resulting κ_{rad} steeply increases from 1.2 W/(m·K) at 1000 K to 1.9 W/(m·K) at 1500 K for (001) of olivine Fo_{90} (Fig. 1). These values are inconsistent with the measured total conductivity of 3.1 to 3.3 W/(m·K) under the same conditions (*4*) or with polycrystalline κ [which remains near 2.8 W/(m·K) (*24*)] in that κ_{lat} is expected to vary as $1/T$ (*10*), implying that the change in κ_{rad} over this range would increase by 30% rather than by 60%. High values were calculated for κ_{rad} from measured absorbance (*23*) because using $\lambda = A - 1$ accounts only for direct transitions at the center of the Brillouin zone and neglects most interactions of light with phonons, that is, those scattering events involving a reciprocal lattice vector.

Here, I develop a model for κ_{lat} at ambient conditions on the basis of parameters obtained from reflectance spectra. The calculations are shown to be in excellent agreement with experimental data on mantle minerals. General relations deduced for the temperature and pressure dependences of κ_{lat} are shown to agree with experimental results for salts, silicates, and oxides. A similar model is presented for κ_{rad}. The results are then used to set limits on the lithosphere and mantle geotherms and conductivity.

Theory

Ambient conditions. Lifetimes are implicit in reflectance spectra, as derived from classical dispersion analysis. In this model, IR reflectivity is calculated assuming a collection of damped harmonic oscillators with frequency ω_i,

---

Department of Earth and Planetary Science, Washington University, St. Louis, MO 63130, USA. E-mail: hofmeist@levee.wustl.edu

damping coefficient Γ_i, and oscillator strength f_i (*25*). The phonon lifetime nearly equals $1/\Gamma_i$ (*26*); in many cases, this is exact (*27*). Sometimes Γ_i is even referred to as the relaxation frequency (*21*). For $\Gamma_i/\omega_i \ll 1$, as is usually the case, Γ_i is the full width at half-maximum (FWHM) of the peak in ε_2, the imaginary part of the dielectric function (*27*). Insignificantly different values of Γ_i are obtained from Kramers-Kronig analyses of reflectance (*28, 29*).

For frequency regions with no phonons, the dielectric function is real, and $u_i = \omega_i/q_i = c/n(\omega_i)$, that is, the group velocity equals the phase velocity (*26*), where n is the index of refraction and c is the speed of light. Such high velocity does not exist at frequencies where IR light is absorbed; instead, u_i approaches zero, as can be seen in inelastic neutron scattering (INS) measurements (*30*) and in theoretical dispersion curves [see (*10, 26*)] both at the center of the Brillouin zone ($q_i = 0$). Ideally, INS data could be used to obtain the average slope over the first Brillouin zone: For cubic symmetry,

$$u_i = d\omega_i/dq_j \approx [\omega_i(0) - \omega_i(2\pi/a_j)]/(2\pi/a_j) = a_j\Delta\omega/2\pi \qquad (4)$$

where a_j is a lattice constant. However, INS data for solids of geophysical interest are rare and generally incomplete (*31*). Therefore, I approximate the frequency shift over the Brillouin zone $\Delta\omega$ (the dispersion) by averaging the difference between the transverse optic (TO) frequency of the ith mode and its longitudinal optic (LO) frequency with the difference between this same TO frequency and the LO frequency of the adjacent jth mode. [For $\Gamma_i/\omega_i \ll 1$, ω_i is the TO$_i$ frequency and the LO$_i$ frequency is a function of ω_i, Γ_i, and f_i (*27*).] This approximation is derived by inspection of experimental and theoretical dispersion curves. Most minerals have a large number of modes, giving low dispersion, and thus this approximation adds little uncertainty (probably a few percent). In effect, the summation of Eq. 2 smooths the data.

If Eq. 2 is to be applied at ambient conditions, the IR modes must be assumed to represent all optic modes of the crystal. This approximation for the density of states was used by Kieffer (*32*) in C_P calculations, which are accurate within a few percent near 298 K. For mantle minerals (which typically have a large number of modes), the distributions of Raman and IR frequencies compare closely, and symmetry analysis suggests similar behavior for inactive modes (*33*).

The three acoustic modes are enumerated separately. Their group velocities equal the speeds of the one compression (longitudinal) and two shear (transverse) waves, u_P and u_S (*32*). FWHM values from sideband spectra (*34*) can be used to approximate the lifetimes.

Thus, calculation of κ_{lat} at ambient conditions requires knowledge of density (*12*), the TO$_i$ = ω_i and LO$_i$ frequencies and Γ_i from IR reflectance spectra, acoustic velocities, acoustic peak widths, lattice constants, and molecular weight. Computation of D requires heat capacity, which can also be calculated from IR spectra (*32*).

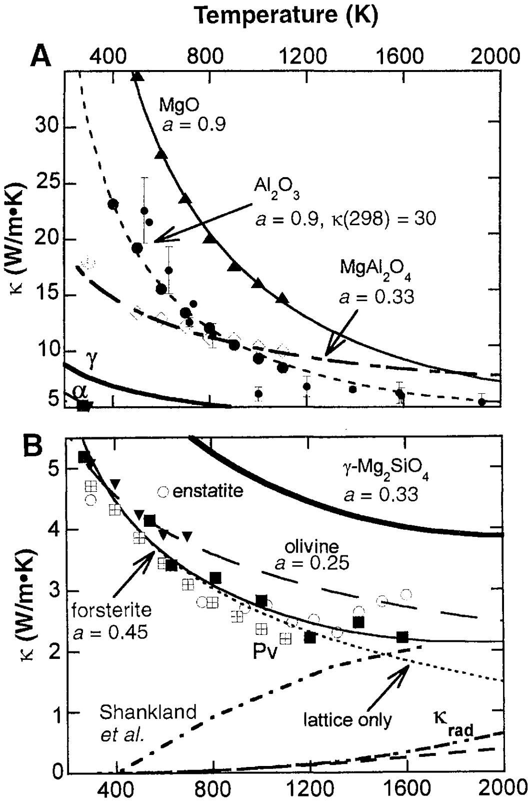

Fig. 1. Thermal conductivity versus temperature. (**A**) Mostly oxides; (**B**) mantle silicates (note the difference in y-axis scales). Data from conventional measurements (*3*): ▲, MgO; ●, Al_2O_3; ◇, spinel; ▼, olivine. Data from laser heating (*18*): small dots with error bars, Al_2O_3; ■, Fo; ○, enstatite having ~0.19 Fe/(Mg + Fe). Shaded circle at left in (A), room-temperature κ for corundum (*51*); ⊞, Pv κ calculated using D from 100 to 400 K from (*61*), $C_P(T)$ from (*63*), and $V(T)$ from (*62*). Dot-dash line, previous radiative contribution for olivine (*23*). Dot-dot-dash-dash line, radiative contribution calculated for Fo from overtone lifetimes. Medium-dashed line, radiative contribution calculated for olivine from overtone and Fe^{2+} lifetimes. Dotted line, Fo fit to lattice contribution only. Long-dashed line, olivine fit to radiative contribution (including Fe effects). All other lines are lattice contribution plus radiative contribution from overtones fit to the various minerals by varying a values, as labeled. For corundum, κ(298) was fitted to 30 W/(m·K) to match the high-T measurements, instead of using data from (*51*). Heavy solid line, γ phase; κ(298) was calculated from IR reflectivity (*54*), and a was assumed to equal that of the silicates and spinel.

The radiative contribution and its temperature dependence. It is immaterial whether transitions involve electronic or vibrational excitations; both can be described as damped harmonic oscillators (*21, 26, 27*). Thus, $\lambda = u\tau = u/\Gamma$, where Γ is also obtained from FWHM from the dielectric function at appropriately high frequencies. Bands in the near-IR to visible are relatively weak; for this case, the group velocity u is approximated as its maximum value of c/n. Scattering is neglected because it is minor compared to absorption (*20, 23*). Because reflectivity at appropriate frequencies is lacking for mantle minerals, Γ_i is approximated from absorbance widths. If Γ is roughly the same for all peaks and independent of temperature, then Eq. 3 reduces to Clark's (*20*) result, slightly modified:

$$\kappa_{rad} = 16\sigma T^3\lambda n^2/3$$
$$= 16\sigma T^3 cn/3\Gamma = bT^3 \qquad (5a)$$

where σ is the Stefan-Boltzmann constant and b is a fitting parameter. If Γ varies with ω, then Eq. 3 can be evaluated as a sum of integrals over different frequency regions using tabular data [for example, (*20*)]. For this case, the result can be fit to a polynomial series:

$$\kappa_{rad}(T) = \Sigma b_i T^i = f(T) \qquad (5b)$$

Effect of pressure and temperature on the lattice contribution. The pressure and temperature dependence of κ_{lat} is contained in the frequencies and damping coefficients of the modes, as these are largely dependent on the volume V. To obtain a useful parameterization of $\kappa_{lat}(P,T)$, I recast Eq. 2 in terms of ω_i, Γ_i, and volume. For the following derivation, the two assumptions made above to calculate κ_{lat} at ambient conditions are not needed. Specifically, the sum is now taken over all vibrational modes (not just IR and acoustic) and an exact form is now used for the dispersion relations. The following relations pertain: (i) The sound speeds are proportional to the acoustic frequencies multiplied by a lattice constant (*32*). (ii) The group velocity of the optic modes is also proportional to the frequency times the lattice constant (*26*); the specific relation derived from complex variables is immaterial. (iii) The pressure derivative of the factor $\exp(x_i)/[1 - \exp(x_i)]^2$ is small (that is, the numerator and denominator roughly cancel) relative to those of the other terms and can thus be ignored. (iv) Γ_i is independent of pressure, as indicated by the constant LO-TO splitting in alkali halides (*35*). (v) For $T > 298$ K, the factor $\exp(x_i)/[1 - \exp(x_i)]^2 \approx T^2$ and thus cancels the $1/T^2$ from the prefactor (x_i^2) of c_{ij}. Thus, density times Eq. 2 [see (*12*)] reduces to

$$\kappa_{\mathrm{lat}}(P,T) \propto V^{1/3}\Sigma\omega_i^4/\Gamma_i \quad (6)$$

To obtain derivatives, I assumed that the mode Grüneisen parameters $\gamma_i = (\omega_i/K_T)\partial\omega_i/\partial P$ (where K_T is the bulk modulus) are similar and nearly equal to the average $\langle\gamma_i\rangle$, which is equated to $\gamma_{\mathrm{Th}} = \alpha V K_T^2/C_V$, where α is thermal expansivity [for example, (*34*)]. The damping coefficients are similarly averaged. Thus,

$$\frac{\partial[\ln(\kappa_{\mathrm{lat}})]}{\partial P} = \frac{1/3 + 4\gamma_{\mathrm{Th}}}{K_T} \quad (7)$$

and

$$\frac{\partial[\ln(\kappa_{\mathrm{lat}})]}{\partial T} = -\frac{\alpha}{3} + \left\langle\frac{4}{\omega_i}\frac{\partial\omega_i}{\partial T}\right\rangle - \left\langle\frac{1}{\Gamma_i}\frac{\partial\Gamma_i}{\partial T}\right\rangle$$

$$= -\alpha\left(4\gamma + \frac{1}{3}\right) - \left\langle\frac{1}{\Gamma_i}\frac{\partial\Gamma_i}{\partial T}\right\rangle \quad (8)$$

where the angle brackets indicate an average. To obtain the right side of Eq. 8, I assumed that γ_{Th} is independent of P and T. High-order derivatives of κ_{lat} are negligible (*36*).

Integrating Eq. 8 gives

$$\kappa(T) = \kappa(298)\frac{\Gamma(298)}{\Gamma(T)} \times \exp\left[-\left(4\gamma_{\mathrm{Th}} + \frac{1}{3}\right)\int_{298}^{T}\alpha(\theta)d\theta\right] \quad (9)$$

The integral does not begin at 0 K because of a singularity and because the above derivation requires $T > 298$ K. Because data on the temperature dependence of Γ are scarce (essentially nonexistent for minerals), the term $\Gamma(298)/\Gamma(T)$ is approximated as $(298/T)^a$, where a is a fitting parameter. This approximation is based on existing spectral data (*23*, *37*). The $c_1 + c_2/T$ dependence for κ_{lat} surmised previously (*13*, *25*) is a special case of Eq. 9.

For mantle conditions, the thermal conductivity is approximated by integrating Eqs. 7 and 9 and combining the result with the generalized form of κ_{rad}, Eq. 5b (*38*):

$$\kappa(P,T) = \kappa(298)\left(\frac{298}{T}\right)^a \times \exp\left[\frac{4qP}{K_0'} - \left(4\gamma_{\mathrm{Th}} + \frac{1}{3}\right)\int_{298}^{T}\alpha(\theta)d\theta\right] \times \left(\frac{K_0 + K_0'P}{K_0}\right) \times \exp\left[\frac{4\gamma_{\mathrm{Th}} + 1/3}{K_0'} - \frac{4qK_0}{(K_0')^2}\right] + f(T) \quad (10)$$

where $K_0' = dK_T/dP$ is assumed to be constant, the temperature and pressure dependences of K_T are assumed to be independent, and $q = d\gamma/dP$. For mantle substances, $\gamma_{\mathrm{Th}} =$ 1 to 1.4, $K_0' =$ 4 to 5, and $q \approx 0$. Within the uncertainty of these parameters, Eq. 10 simplifies to

$$\kappa(P,T) = \kappa(298)(298/T)^a \times \exp[-(4\gamma + 1/3)\int\alpha(\theta)d\theta] \times (1 + K_0'P/K_0) + f(T) \quad (11)$$

Results

Ambient conditions. Only a few mantle materials have both the IR reflectance spectra and accurate conductivity measurements needed to test the theory at 1 atm and 298 K. For olivine (*39*) I fit the IR spectra for each polarization with a classical dispersion analysis, which includes nonzero angles of incidence, using fayalite (Fa) parameters (*28*) as a starting point. Frequencies shift with the Fe content but differ only slightly from results on Fo (*40*). Widths appear independent of Fe content. Using these data in Eq. 2 yields $\kappa = 4.61 \pm 0.08$ W/(m·K) for Fo_{90}, in which the acoustic modes contribute 45%. This is close to the PTGS determination of 4.78 ± 0.09 W/(m·K) (*6*) and to the average from conventional methods of 4.65 W/(m·K) (*41*).

For mantle garnet, an IR spectrum (*42*) was used for a chemical composition very close to that studied by PTGS (*6*). The result, 3.28 ± 0.02 W/(m·K) (with the acoustic modes contributing 27%), equals the PTGS value of 3.29 ± 0.09 W/(m·K) (*6*) and conventional measurements of 3.2 W/(m·K) for a pyrope-almandine (*41*). Uncertainties for the calculation are less for garnet because the acoustic peak widths were constrained by sideband spectra of pyrope (*34*), whereas those of olivine were estimated from other mineral families and also because the proportion of acoustic modes is larger for olivine modes (81 optic modes for olivine compared with 237 for garnet; both have three acoustic modes).

These examples show that the calculation is accurate at ambient conditions and that the optic modes transport most of the heat through the crystal. One other mineral, enstatite, was studied by PTGS (*6*), but single-crystal IR spectra are unavailable.

Pressure derivatives. Experimental determinations of $\partial[\ln(\kappa)]/\partial P$ are reliable only for olivine using PTGS (*6*), and for soft solids such as NaCl and $\mathrm{NaClO_3}$ using conventional techniques (*2*). Slopes calculated using Eq. 7 lie within the experimental uncertainty of these measurements (Table 1). Conventional measurements of $\partial[\ln(\kappa)]/\partial P$ for hard solids are problematic (*9*) and thus neither prove nor disprove the model. However, averages of multiple measurements for the various minerals bracket the calculation (Table 1). Often, the lowest slope from conventional measurements is closest to the calculation, consistent with overestimation of κ at high pressure due to the loss of thermal contact upon cracking.

Temperature dependence. Analysis of $\kappa(T)$ must be done with care because conventional measurements up to 1100 K (*3*, *41*) show variable behavior. Minima (for example, enstatite in Fig. 1) are not consistently observed for a variety of substances (*41*) and appear to be affected by variables such as grain size, oxidation (*23*), and experimental configuration [for example, (*4*, *24*)]. Therefore, the data examined here were corroborated by several measurements.

The radiative contribution for olivine is estimated as follows. Comparison of olivine mid-IR dielectric functions (*28*, *40*) to absorption data (*28*) suggests that Γ is about one-third the width of the absorption peaks of the Si-O fundamentals. Absorption peak widths are near 250 $\mathrm{cm^{-1}}$ above 1700 $\mathrm{cm^{-1}}$ (*23*), but Γ values for peaks between 1700 and 1000 $\mathrm{cm^{-1}}$ for Fa range from 40 to 90 $\mathrm{cm^{-1}}$ [extracted from published reflectivity (*28*)]. Higher order overtones ($\omega > 2500$ $\mathrm{cm^{-1}}$) are poorly resolved (*23*) and cannot be used to extract widths. Statistical thermodynamics gives similar partition functions for both blackbody radiation and excitation of vibronic transitions (*43*), which means that the shift in population of the vibronic overtones parallels the shift of the peak of the blackbody curve to higher ω with T (*44*). Most likely, the blackbody light is produced by high-order vibronic transitions. This deduction, coupled with stimulation of transitions by the light (*45*), means that at any given temperature, any transparent region that might exist would be found at frequencies above the region occupied by the blackbody curve. For the near-IR, $n \approx 1$ (*28*, *40*), but in the visible, n rises to 1.6. Using an average n and $\Gamma \approx 50$ $\mathrm{cm^{-1}}$ (as a lower bound for the first-order overtones) for all wavelengths in Eq. 5a yields an upper limit for b of 8.5×10^{-11} W/(m·K) (Fig. 1) for Fo. This estimate also holds for other Fe-free silicates as well as oxides (*46*).

For olivine, the visible region ($\omega > 6000$ $\mathrm{cm^{-1}}$) has multiple absorption peaks from electronic transitions of $\mathrm{Fe^{2+}}$, with widths of about 2000 to 3000 $\mathrm{cm^{-1}}$ (*47*). A Γ value of 600 $\mathrm{cm^{-1}}$ is a reasonable lower limit for visible frequencies at room temperature. Using the above result for vibronic modes, tables of partial Planck functions (*20*, *21*), and the larger Γ at high ω gives an upper limit (*48*) from Eq. 5b for ferrous minerals of

$$\kappa_{\mathrm{rad}} = 0.01753 - 0.00010365T + 2.2451T^2/10^7 - 3.407T^3/10^{11}\ \mathrm{W/(m{\cdot}K)} \quad (12)$$

This representation (Fig. 1) only slightly affects κ below 2000 K.

Equation 9 for the lattice contribution plus $\kappa_{\mathrm{rad}} = 8.5T^3/10^{11}$ W/(m·K) describes the available data for dense silicates and oxides reasonably well (*49*). Several examples are shown in Fig. 1; for all of these, the parameterization of $\alpha(T)$ is from Fei (*50*) and values at 298 K from Horai (*51*) were used except for corundum. The fitting parameter a is largest, ~0.9, for MgO. This result is consistent with the inverse temperature dependence previously inferred for simple substances (*13*). For corundum, the data (*3, 18*) are not consistent with values at 298 K (*51*); the cause for the discrepancy is unclear, but its existence requires that the room-temperature κ be used as a fitting parameter. The high-T data can only be matched by $\kappa(298) = 30$ W/(m·K) and $a = 0.9$. These two parameters do not appear to depend on each other. The parameter a apparently decreases as the proportion of acoustic modes decreases (that is, as the number of atoms in the unit cell increases); $a = 0.9$ for MgO, for which half the modes are acoustic, but $a = 0.45$ to 0.25 for spinel and silicates (Fig. 1).

The parameter a is constrained by the initial slope (Fig. 1) and thus is independent of any form used for the radiative contribution, because both previous (*18–23*) and present calculations show that κ_{rad} is negligible for $T < 500$ K. My model shows that the lattice contribution dominates transport of heat up to 3000 K, consistent with low values of κ_{rad} (Fig. 1) as inferred above. Furthermore, $a = 0.33$ can be used for all silicates, in that available measurements for silicates all follow roughly the same trend (Fig. 1) and because thermal expansivity values vary little among silicates.

Calculation of Conductivity and a New Geotherm

Methodology. The conductivity of the layers in Earth was determined by summing the pressure and temperature dependence of the constituent mineral phases in proportion to their abundances. For each zone above 670 km, I used average abundances of olivine or ringwoodite (Fe-bearing γ-Mg_2SiO_4), garnet, orthopyroxene (Opx), and clinopyroxene (Cpx) for each of the various compositional models from (*52*). I used the initial values in Table 1 (*53*) and thermal expansivity compiled by Fei (*50*). For ringwoodite, κ at 298 K was calculated as 7.7 W/(m·K) from IR reflectivity (*54*). This high value is supported by a similar difference in κ between α- and γ-Fe_2SiO_4 (*55*) and by large κ for spinel sensu stricto (*3, 51*). Mantle iron contents of 10% are assumed to lower κ by 0.5 W/(m·K) from the Mg end-member, as observed for various silicates (*51*).

The thermal conductivity of oxides depends much more strongly on temperature ($a = 0.9$; Fig. 1) than that of the silicates; hence, using only oxide data to infer lower-mantle conditions as in (*56*) is unsupported. Furthermore, Manga and Jeanloz (*56*) used overly large pressure derivatives for thermal conductivity of MgO [data of (*57*) rather than (*58–60*)]. Earlier models (*15*) also used very large pressure derivatives. Here, perovskite (Pv) κ is based on available data (*61–63*), using Eqs. 11 and 12 with $a = 0.33$. This value is justified both by Pv having a large proportion of IR modes and by the slope near 298 K (Fig. 1B). Lower-mantle conductivity is then obtained by proportionating Pv and magnesiowüstite (Mw) values.

The values for $\kappa(P,T)$ depend on the geotherm $T(P)$, and for the conductive outer shell

Table 1. Pressure dependence of thermal conductivity and ambient values. The last digit is uncertain by ±1 unless indicated. Assumed values for K' are denoted by ≡.

Structure	Composition	Thermal properties			Calculated $\partial[\ln(\kappa)]/\partial P$ (GPa^{-1})	Measured		
		γ_{Th}*	K_T* (GPa)	K'*		$\partial[\ln(\kappa)]/\partial P$ (GPa^{-1})	κ (ambient) [W/(m·K)]	Reference
Olivine	Fo = Mg_2SiO_4	1.25	127.9	4.0	0.0417	0.18¶	5.2#	(*55*)
Olivine	$Fo_{90}Fa_{10}$	1.28	128.1	4.6	0.0426	0.04	4.7	(*6*)
						0.046	5.0#	(*24*)
						0.06		(*92*)
						0.165¶		(*93*)
Olivine	Fa = Fe_2SiO_4	1.45	135.1	≡4	0.0454	–	3.16	(*51*)
Garnet	$Mg_3Al_2Si_4O_{12}$	1.43	171.5	3.8	0.0353	–	3.2 (some Fe)	(*51*)
Garnet	$Mg_{1.5}Fe_1Ca_{0.5}Al_2Si_4O_{12}$	~1.4	169.5	4.09	~0.035	–	3.3	(*6*)
Opx	$MgSiO_3$	0.96	107	5–10	0.039	0.07	4.5‡‡	(*94*)
Cpx	$CaMgSi_2O_6$	0.90	112	4.7	0.035	–	4.9 (average)	(*51*)
β	Mg_2SiO_4	1.0†	172	4.8	0.025	–	–	
γ	Mg_2SiO_4	1.25	183	5.2	0.029	–	7.7 (calc.)	See text
Garnet	$MgSiO_3$	1.33	154	≡5	0.0369	–	–	
Ilmenite	$MgSiO_3$	1.70‡	210	≡5	0.0339	–	–	
Pv	$MgSiO_3$	1.2–1.7§	261	≡5	0.025(2)	–	4.7	§§
Stishovite	SiO_2	1.2‖	306	2.8	0.026	0.090**	1.7**	(*57*)
							8.6	(*95*)
Coesite	SiO_2	0.41	113	8.4	0.017	0.01–0.04	1.4–1.5	(*92*)
						0.039**	8.0**	(*57*)
Quartz (⊥c)	SiO_2	0.667	37.5	6.4	0.080	0.017	7.7#	(*92*)
						0.17**		(*57*)
						0.17**		(*96*)
						0.25		(*97*)
Rocksalt	MgO	1.54	160	4.3	0.041	0.02		(*58*)
						0.04		(*60*)
						0.05	55.2	(*59*)
						0.068**	41**	(*57*)
Spinel	$MgAl_2O_4$	1.4	195.2	4.9	0.030	–	9.5	(*51*)
Corundum	Al_2O_3	1.27	255.4	4.3	0.021	–	18	(*51*)
Rocksalt	NaCl	1.58	23.8	4.45	0.280	0.32(4)††	6.6#	(*2*)
Oxysalt	$NaClO_3$	1.85	24.6	≡4	0.206	0.22	1.0	(*98*)

*From (*88*) unless noted. †From (*89*). ‡Used thermal expansion from Ashida *et al.* (*90*). §The range exists because thermal expansion values (*62*) depend on whether volume above or below room-temperature experiments is used. ‖From (*91*). ¶These studies are discounted because the results are not consistent with other studies, particularly with PTGS data (*6*) or with the average for NaCl. #The 1-atm value is from (*51*) rather than the referenced study at pressure. **Because substantial cracking was observed, the results are unlikely to be accurate. ††Average of six experiments, not including (*55*) from Ross *et al.*'s (*2*) compilation. ‡‡For Opx with 10% Fe, κ values are 4.2 (*55*), 4.4 (*4*), or 3.46 W/(m·*K*) (*6*). §§Calculated from Osaka and Ito's (*61*) diffusivity; see Fig. 1. The ambient value resembles those of other dense Mg silicates.

the results are interdependent. Linear temperature profiles previously derived for old oceanic crust and lithosphere (*64*) result from assuming that κ is constant when solving Eq. 1, which was justified by the opposing effects of T and P. However, the decrease in κ with temperature dominates in the crust and lithosphere. Thus, to determine $\kappa(P,T)$ in the oceanic lithosphere away from the ridges, we solve Eq. 1 using boundary conditions at the surface, where heat flow $Q_0 = 0.05$ W/m^2 and $T_0 = 277$ K (*65*). An analytical solution is not possible because the variables cannot be separated. For the outer layers, a finite solution was obtained by numerical integration over a limited depth range of about 25 km (*66*) using $dP/dZ = 0.0329$ GPa/km from the Preliminary Earth Reference Model (*67*).

Temperatures and thermal conductivity in the oceanic lithosphere. The initial slope of the conductive geotherm matches that obtained from constant κ (*64*). By 20 km, however, the new geotherm is hotter and increasingly steepens (Fig. 2A). The numerical result for Z below 120 km is represented by

$$T = 277 + 12.297Z + 0.05733413Z^2 \tag{13}$$

Because the measured temperature dependences of thermal conductivity for dense silicate minerals are nearly equal (Fig. 1) and ambient κ values for silicates are similar (Table 1), the uncertainty in the geotherm is low, probably a few percent.

High temperatures result from inefficient conduction in the deep lithosphere. The new conductive geotherm attains 1440 K at 70 km, where it intersects the solidus of pyrolite with 8.3 weight % H_2O (*68*). This intersection equals, within the uncertainty, the thickness of old Pacific plate defined seismically, 68 km (*69*). Near the Tonga trench, for example, velocity differences indicate that partial melting could exist at shallow depths of 30 to 90 km (*70*), consistent with the high calculated temperatures and narrow slab thickness (*69*). At 1675 K and 81 km (Fig. 2A), the geotherm intersects the dry solidus of peridotite (*71*). This position, too, is consistent with seismic data in that the conductive profile should include whatever thermal boundary layer exists below the rigid lithosphere. In the lithosphere, thermal conductivity decreases to 2.7 W/(m·K) at 64 km, and it may be as low as 2 W/(m·K) if the thermal boundary layer extends to 81 km (Fig. 3).

Temperature in the mantle. A mantle geotherm can be inferred from the conductive cooling curve of old oceanic lithosphere, phase equilibria, and seismic constraints. If the low-velocity zone (LVZ) is partially melted, then the geotherm follows a solidus (Fig. 2B): The LVZ is terminated where the solidus intersects the mantle adiabat. This depth is taken as the halt in the decrease in seismic velocity at 200 km rather than the average basal depth of 225 km (*67, 69, 70*). Two limiting cases are consistent with the oceanic geotherm:

1) If the LVZ is anhydrous, then the dry solidus (*71*) requires a globally averaged temperature of 2020 K. An uncertainty of 50 K stems from the range of basal depths from 180 to 225 km. The temperature in the upper mantle rises adiabatically with depth; 0.33 K/km (*72*) was used. For the case of whole-mantle convection, the lower mantle follows the same adiabat. Extrapolation to the core-mantle boundary (CMB) gives a temperature of 2830 K, which is 230 K higher than recent deductions (*73*). For this hot and dry case, I also consider the additional possibility of layered convection, for which the adiabat in the upper mantle and transition zone is terminated by a boundary layer, ostensibly the 670-km discontinuity. The temperature at the top of the lower mantle could be defined by a triple point involving Pv (*74–76*), making this seismic discontinuity sharp. The garnet-ilmenite-Pv triple point (*74*) is adopted because it falls in the middle of available data (Fig. 2B) and lies below the pyrolite solidus (*77*). An adiabat through this triple point attains 3050 ± 100 K at the CMB.

2) If water is present in the LVZ, melting occurs at lower temperatures. It is likely that dehydration progresses with depth, and hence the temperature would ascend through the solidi determined for decreasing water content as P increases. For simplicity, I assume that the temperature falls on a straight line defined by the conductive temperature of 1440 K at the 68-km seismic constraint and the intersection of the γ = Pv + Mw phase equilibria with 670 km at 1870 K. The lower-mantle adiabat inferred by Ito and Katsura is then followed (*73*). Although this approximation is not adiabatic in the upper mantle, it lies close to the intersection of the α-β transition (*78*) with 410 km, and it provides a lower limit to the mantle temperature because it assumes that the thermal boundary layer is no thicker than the rigid lithosphere.

The two dry mantle geotherms (whole or layered convection) bracket the mantle temperatures deduced by Stacey (*79*) on the basis of thermodynamic principles and equations of state. Subsequent inferences of colder mantle geotherms (*73, 80*) can be reconciled with the hot, thin lithosphere if temperatures in the LVZ are governed by a progression of wet solidi. I do not suggest that water contents reach 8 weight %, but rather, the point here is to explore the range of thermal con-

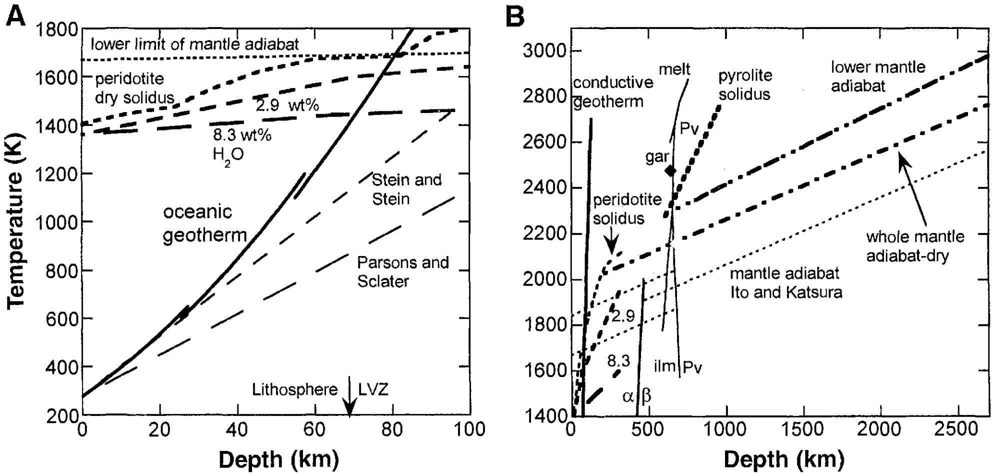

Fig. 2. Geotherms and phase equilibria in the lithosphere (**A**) and mantle (**B**). Light long-dashed lines, previous results for $T(P)$, assuming that κ is constant (*64*). Heavy solid lines, $T(P)$ for conductive cooling from Eqs. 1, 11, and 12. The breaks show the depth intervals used over which $\kappa(P)$ was assumed to take the average value. Short-dashed line, dry solidus of peridotite (*71*). Heavy long-dashed lines, wet solidus of pyrolite for 2.9 and 8.3 weight % water (*68*). The depths of intersection of the new geotherm with the various solidus curves are comparable to the depth of the old oceanic lithosphere [arrow in (A)] from seismic observations (*69*). Dotted lines, possible mantle adiabats based on the intersection of the γ = Pv + Mw phase boundary with the 670-km discontinuity (*73*); the most probable adiabat is shown extrapolated through the deep mantle, whereas the range of adiabats is shown in the upper mantle. Heavy dot-dashed line, mantle adiabat defined by a slope of 0.33 K/km (*72*) with the starting point at an average 200-km basal depth of the LVZ, which lies on the peridotite dry solidus. Light solid lines, phase equilibria involving the Mg end-member of Pv (*74*). Medium solid line, the α-β phase transition in Mg_2SiO_4 (*78*). Heavy short-dashed line, solidus of pyrolite (*77*). ◆, the triple point involving the Pv phase for $(Mg_{0.9}Fe_{0.1})SiO_4$ (*76*); ◇, the triple point involving Pv for end-member Mg_2SiO_4 (*75*). Heavy dot-dot-dash-dash line, possible hot adiabat for the lower mantle.

ductivities implied by reasonable minimum and maximum mantle temperatures.

Thermal conductivity in the mantle. The total conductivity for the mantle (Fig. 3) was calculated for the various geotherms discussed above. The relative invariance in the P derivatives (Table 1) and the similar values of κ attained at high temperature (for example, Fig. 1) provide total conductivity in the upper mantle that is roughly independent of mantle mineralogy: Even the presence of large amounts of garnet, with its relatively low thermal conductivity, makes little difference (Fig. 3). However, a spread in κ is possible in the upper mantle because the minimum in κ occurs at the base of the thermal boundary layer at the top of the convecting mantle: The lowest value attained for κ depends on how deep this layer extends below the rigid lithosphere. The curves for pyrolite in Fig. 3 indicate the range of κ for the possible geotherms.

In the transition zone, uncertainties result from the possible temperatures, and in addition, the amount of ringwoodite matters considerably, because it has a high thermal conductivity. If changes in mineralogy with depth [for example, (*52*)] were included, then the $\kappa(P)$ curves in the transition zone would be about 10% steeper than those shown in Fig. 3, such that the value at the midpoint remains the same. Accounting for this possibility lessens the discontinuities in κ for most of the mineralogical models.

For the lower mantle, the appearance of Mw increases κ (Table 1). Because the rate of change of κ with temperature is low in the inferred temperature range and because Mw is only 20% of the total mineralogy, the resulting slope in the lower mantle is comparable to that of the upper mantle and transition zone (Fig. 3). Furthermore, because the lattice and radiative contributions to κ oppose each other, the values of κ in the lower mantle are not terribly influenced by the geotherm. The discontinuity in κ at 670 km depends on both the mineralogy in the transition zone and the assumed geotherm.

The total conductivity in D'' (Fig. 3) was calculated assuming that a conductive gradient occurs between 2680 and 2880 km such that the temperature at the top of D'' varies as shown in Fig. 2, but with T equal to 3900 K at the CMB for all models (see below). The steep decrease in κ occurs because the change is temperature-driven and because the radiative contribution is small and increases slowly at high temperatures.

The radiative contribution (Fig. 3) is relatively small across the mantle, reaching 0.67 to 0.82 W/(m·K) (10 to 15% of the total κ) at the core, depending on the geotherm. Hence, the lattice contribution dominates, yielding κ_{tot} = 5.8 to 6.7 W/(m·K) at the top of D''. Thermal conductivity is unlikely to lie outside of this range. First, the corresponding high temperature approaches the lower limit of core melting at 3300 ± 200 K (*81*). Although including the second-order derivative (Eq. 10) would decrease the minimum (by 10% if q is large, near unity), the radiative contribution for Mw may have been underestimated near 3000 K, as suggested by the slight mismatch near 1500 K, and a small increase would offset the decrease. Second, if lower temperatures than the proposed minimum are used—for example, the lower limit of mantle adiabat from (*73*)—then κ would be 7.5 W/(m·K). In this case, curvature (Eq. 10) would more than negate such an increase, whereas the radiative contribution at this lower temperature of 2500 K could not have been underestimated by as large an amount.

Ramifications of the model. The results can be used to infer the conductive power output of the core. Recent considerations of the core adiabat give 3800 to 4000 K at its outer surface (*82*), implying that the jump across the 200-km-thick D'' layer is 1300, 1100, or 900 ± 100 K for the three geotherms (Fig. 2B), corresponding to κ = 5.8, 5.6, and 5.5 W/(m·K) in D'' (Fig. 3). The lowest ΔT = 900 K agrees with the independent derivation of 840 K (*83*). For a conductive boundary layer, the power output of the core from Eq. 1 is the absolute value of the area $\kappa\Delta T/\Delta Z$, giving 5.7, 4.7, and 3.8 TW for the three geotherms, with uncertainties of 10 to 15%. All values lie within the uncertainty of independent estimates of 1 to 10 TW for the heat emitted from the core [for example, (*84–86*)], but the best match is obtained between a hot, dry mantle and the recent result of Anderson (*86*). The agreement suggests that D'' is a stable boundary layer.

The pressure and temperature dependence of κ pertains to the style of convection. The Rayleigh number R_{B} equals $g\alpha\Delta T d^3/D\eta$, where η is viscosity, g is the gravitational constant, and d is the thickness of the layer. The geotherms based on a dry solidus in the LVZ (Fig. 2B) are considered here. For the upper mantle, ΔT in excess of the adiabat is about 2100 K. Using this, an average κ of 3 W/(m·K), and an average $\eta = 3 \times 10^{21}$ Pa·s (*87*) gives $R_{\mathrm{B}} = 2.3 \times 10^{6}$. For whole-mantle convection, ΔT is 2900 K (to include the gradient across D''), κ averages 4.3 W/(m·K), and η averages 2×10^{22} Pa·s, giving $R_{\mathrm{B}} = 2 \times 10^{7}$. For the lower mantle, ΔT is ~100 K from the discontinuity near 670 km plus 900 K for D'', κ = 4.5 W/(m·K), and $\eta = 3 \times 10^{22}$ Pa·s (*87*), and thus $R_{\mathrm{B}} = 1.2 \times 10^{7}$. The average thermal conductivities (Fig. 3) on which these estimates are based do not strongly depend on the possible geotherms (Fig. 2B) or mantle mineralogies, suggesting that the upper mantle alone could convect vigorously. The Prandtl number, η/D, of the lower mantle is about six times that of the upper mantle, and the aspect ratios are dissimilar; these factors may also contribute to layered convection. The absence of an obvious barrier to transport across 670 km suggests that circulations in the upper and lower mantle would be coupled.

The specific geotherm affects mineralogical models of the mantle above the 670-km discontinuity. The 410-km discontinuity cannot be reconciled with the olivine to a spinel (α-β) transition for any of the

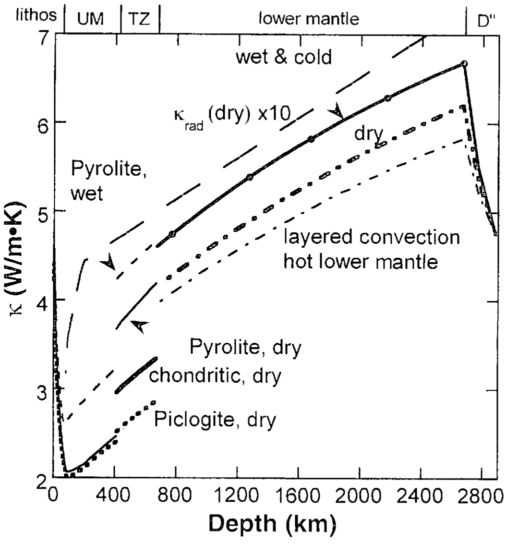

Fig. 3. Thermal conductivity versus pressure. See text and Fig. 2 for model geotherms used to calculate κ. Long-dashed line, radiative contribution multiplied by 10 for a dry solidus, whole-mantle convection, and the presence of Fe^{2+}. All other lines are total thermal conductivity. The short-dashed lines for the pyrolite model in the upper mantle (UM) and transition zone (TZ) were calculated for wet solidi and decreasing water content with depth. The following upper-mantle and transition-zone curves were calculated using a dry solidus (*71*) in the LVZ: Light solid line, pyrolite model. Dotted line, piclogite model. Heavy solid line, κ for a chondritic mineralogy of (*52*) (for the upper mantle, this is not shown but lies between the curves for piclogite and pyrolite). For the lower mantle, only a chondritic composition (80% Pv, 20% Mw) was considered. Heavy dot-dashed line, lower mantle assuming whole-mantle convection and a dry solidus. Solid line with dots, lower mantle using the adiabat of (*73*), which is probably the lowest temperature possible. Light dot-dashed line, lower mantle allowing the maximum possible temperature and layered convection. The discontinuities in κ at 410 and 670 km are attributable to the high conductivity of ringwoodite.

adiabats in Fig. 2B, because of its substantial Clapeyron slope (*78*). In particular, the low temperatures required for such an assignment are incompatible with the conductive profile in the lithosphere. One possibility is that the 410-km discontinuity involves conversion to the garnet structure. The presence of Al and Ca in the mantle will expand the garnet field to lower pressures than the boundary for pure $MgSiO_3$. This suggestion is based on the observation that seismic velocities in the transition zone are intermediate to those of olivine and garnet [compare (*84*)] and that conversion to garnet in the Mg-Si system involves a steep Clapeyron slope [see (*75*)]. Furthermore, extrapolation of the α-β phase boundary for Mg_2SiO_4 intersects the hot, dry geotherm at 520 km, consistent with this discontinuity's local, rather than global, occurrence. The feasibility of a hot, dry geotherm (Fig. 2B) is suggested by the above inference, the conductive power implied for the core, the high temperatures at the base of the oceanic lithosphere, and the existence of the LVZ. If a hot, dry, layered mantle does exist, then the region from 520 to 670 km, where $\kappa(Z)$ is discontinuously high, might serve as a conductive thermal boundary layer and mixing zone between the upper and lower mantle.

References and Notes

1. H. S. Carslaw and J. C. Jaeger, *Conduction of Heat in Solids* (Clarendon, Oxford, 1959).
2. R. G. Ross, P. Andersson, B. Sundqvist, G. Bäckström, *Rep. Prog. Phys.* **47**, 1347 (1984).
3. H. Kanimori, N. Fujii, H. Mizutani, *J. Geophys. Res.* **73**, 595 (1968).
4. Y. Koyabashi, *J. Phys. Earth* **22**, 359 (1974).
5. G. Bäckström, in *Proceedings of the 7th Symposium on Thermophysical Properties*, A. Cezairliyan, Ed. (American Society of Mechanical Engineers, New York, 1977), pp. 169–180; U. Brydsten, D. Gerlich, G. Bäckström, *J. Phys. C Solid State Phys.* **16**, 143 (1983); O. Alm and G. Bäckström, *J. Phys. Chem. Solids* **35**, 421 (1974).
6. M. Chai, J. M. Brown, L. J. Slutsky, *Phys. Chem. Miner.* **23**, 470 (1996).
7. J. Zaug, E. Abramson, J. M. Brown, L. J. Slutsky, in *High-Pressure Research: Application to Earth and Planetary Sciences*, Y. Syono and M. H. Manghnani, Eds. (Terra, Tokyo, 1992), pp. 157–166.
8. E. H. Abramson, L. J. Slutsky, J. M. Brown, *J. Chem. Phys.* **104**, 5424 (1996).
9. M. D. Collins, J. M. Brown, E. H. Abranson, L. J. Slutsky, *Eos* **79**, F753 (1997).
10. C. Kittel, *Introduction to Solid State Physics* (Wiley, New York, 1976).
11. P. Debye, *Vortrage über die kinetische Theorie der Materie und der Electrizität* (Teuber, Berlin, 1914), pp. 19–60.
12. Because c_{ij} as defined is computed per mole, reporting κ in units of watts per meter-kelvin requires multiplication of Eq. 2 by the density ρ and division by the molecular weight of the compound.
13. For example, J. M. Ziman, *Electrons and Phonons: The Theory of Transport Phenomena in Solids* (Clarendon, Oxford, 1962); G. Liebfried and E. Schlömann, *Nachr. Ges. Wiss. Goettingen Math. Phys.* **K1**, 71 (1954); M. Roufosse and P. Klemens, *Phys. Rev. B* **7**, 5379 (1973); P. Sindzingre and M. J. Gillan, *J. Phys. Cond. Matter* **2**, 7033 (1990).
14. For example, C. L. Julian, *Phys. Rev.* **137**, A128 (1965); P. G. Klemens, *Solid State Phys.* **7**, 1 (1958); M. Roufosse and R. Jeanloz, *J. Geophys. Res.* **88**, 7399 (1983); G. K. White, *High Temp. High Pressures* **21**, 233 (1989).
15. S. W. Kieffer, *J. Geophys. Res.* **81**, 3025 (1976).
16. D. G. Cahill, S. K. Watson, R. O. Pohl, *Phys. Rev. B* **46**, 6131 (1992).
17. J. M. Brown, *Geophys. Res. Lett.* **13**, 1509 (1986).
18. J. F. Schatz and G. Simmons, *J. Geophys. Res.* **77**, 6966 (1972).
19. The linear dependence derived in (*18*) for $\kappa(T)$ results from the form assumed for the lattice contribution. Further, the laser used to heat the sample has a frequency similar to the Si-O stretching modes of the silicates. The presence of an undesirable resonance is suggested by the different behavior seen for Fo and enstatite than for corundum and periclase, in that the latter two materials are not directly stimulated because Al-O and Mg-O fundamentals lie below the laser frequency.
20. S. P. Clark Jr., *Trans. Am. Geophys. Union* **38**, 931 (1957).
21. M. Q. Brewster, *Thermal Radiative Transfer and Properties* (Wiley, New York, 1992), pp. 229–230, 374–382, 385–386, and 424–426; R. Siegel and J. R. Howell, *Thermal Radiation Heat Transfer* (McGraw-Hill, New York, 1972), pp. 468ff and 487.
22. T. Goto, T. J. Ahrens, G. R. Rossman, Y. Syono, *Phys. Earth Planet. Inter.* **22**, 277 (1980).
23. T. J. Shankland, U. Nitsan, A. G. Duba, *J. Geophys. Res.* **84**, 1603 (1979).
24. T. Katsura, *Geophys. J. Int.* **122**, 67 (1995).
25. This method is commonly used to extract peak parameters from solids [for example, W. G. Spitzer, R. C. Miller, D. A. Kleinman, L. E. Howarth, *Phys. Rev.* **126**, 1710 (1962); A. M. Hofmeister and A. Chopelas, *Phys. Chem. Miner.* **17**, 503 (1991)].
26. G. Burns, *Solid State Physics* (Academic Press, San Diego, CA, 1990); to relate Γ_j to τ_j, combine equations 13-19 and 13-27, and compare to equation 9-13.
27. F. Wooten, *Optical Properties of Solids* (Academic Press, San Diego, CA, 1972); A. M. Hofmeister, in *A Practical Guide to Infrared Microspectroscopy*, H. J. Humecki, Ed. (Dekker, New York, 1995), pp. 377–416.
28. This is commonly applied to minerals; see, for example, A. M. Hofmeister, *Phys. Chem. Miner.* **24**, 535 (1997).
29. The value of Γ_j cannot, however, be accurately obtained from absorption peaks because these spectra are not purely TO but also contain some LO contributions [for example, (*25, 27*)]; thus, absorption spectra must be analogously deconvoluted into the dielectric functions to extract Γ_j.
30. TiO_2 [J. G. Traylor, H. G. Smith, R. M. Nickow, M. W. Wilkinson, *Phys. Rev. B* **10**, 3457 (1975)] is one of the few minerals with complete INS data.
31. For example, N. Choudhury, S. Ghose, C. P. Chowdhury, C. K. Loong, S. L. Chaplot, *Phys. Rev. B* **58**, 756 (1998) for enstatite; D. L. Price, S. Ghose, N. Choudhury, S. L. Chaplot, K. R. Rao, *Physica B* **174**, 87 (1991) for Fa; K. R. Rao *et al.*, *Phys. Chem. Miner.* **16**, 83 (1988) for Fo.
32. S. W. Kieffer, *Rev. Geophys. Space Phys.* **17**, 20 (1979) and references therein.
33. See examples in V. C. Farmer, *The Infrared Spectra of Minerals* (Mineralogical Society, London, 1974), and in (*25, 27, 28*).
34. This technique is closely related to Raman spectroscopy. See A. Chopelas, H. J. Reichmann, L. Zhang, in *Mineral Spectroscopy: A Tribute to Roger G. Burns*, M. D. Dyar, C. McCammon, M. W. Schaeffer, Eds. (Geochemical Society, Houston, TX, 1996), pp. 229–242, and references therein.
35. A. M. Hofmeister, *Phys. Rev. B* **56**, 5835 (1997).
36. Differentiating Eq. 6 with respect to *T* gives

$$\frac{\partial^2[\ln(\kappa)]}{\partial T\,\partial P} = \frac{4}{B_T}\frac{d\gamma_{Th}}{dT} + \left(\frac{1/3 + 4\gamma_{Th}}{B_T}\right)\alpha\delta_T \approx 10^{-5}\ \mathrm{K}^{-1}\ \mathrm{GPa}^{-1}$$

where the Anderson-Grüneisen parameter $\delta_T \equiv -(1/\alpha K_T)\partial K_T/\partial T$. Other second-order derivatives of κ are similarly small, as these involve higher order derivatives of the thermodynamic properties. For comparison, $\partial[\ln(\kappa)]/\partial P = 0.04$ GPa^{-1} for olivine (*6*).
37. G. Burns and B. A. Scott, *Phys. Rev. B* **7**, 3088 (1973); A. M. Hofmeister, *Eos* **79**, S163 (1998).
38. The radiative term should be pressure independent, because Γ is pressure independent (*35*), and thus was not integrated over pressure. The change in frequency with pressure is immaterial because the rate of change for the absorption and emission bands would be essentially the same (discussed further below).
39. B. Reynard, *Phys. Chem. Miner.* **18**, 19 (1991).
40. J. L. Servoin and B. Piriou, *Phys. Status Solidi B* **55**, 677 (1973); K. Iishi, *Am. Mineral.* **63**, 1198 (1978).
41. C. Clausner and E. Huenges, in *Rock Physics and Phase Relations: A Handbook of Physical Constants*, T. J. Ahrens, Ed. (American Geophysical Union, Washington, DC, 1995), pp. 105–126.
42. A. M. Hofmeister, unpublished IR data. The spectral parameters are close to other garnets in the middle of the pyrope-almandine binary measured by A. M. Hofmeister, T. J. Fagan, K. M. Campbell, and R. B. Schaal [*Am. Mineral.* **81**, 418 (1996)].
43. F. Reif, *Fundamentals of Statistical and Thermal Physics* (McGraw-Hill, New York, 1965), pp. 251–253.
44. The blackbody radiation is associated with vibronic transitions, implying that high levels must be populated in order for visible light to be given off. The continuum exists because of the large number of overtones and finite widths.
45. For example, at room temperature the first overtone of the Si-O bands is intense at submillimeter thickness (*23*), even though these are expected to be populated at less than 1% of the fundamental population, and the second overtone is also seen but poorly resolved.
46. Because bandwidths on average are about the same for all silicates, the result can be generalized. Oxides have broader mid-IR bands (*33*) and therefore broader overtones than silicates, and could not have higher *b* values. Furthermore, this value for *b* equals the average of the two curves derived for MgO (*22*) by assuming an average absorbance (*20*), which suggests that the above representation is also appropriate for oxides.
47. R. G. Burns, *Mineralogical Applications of Crystal Field Theory* (Cambridge Univ. Press, Oxford, 1970), in particular pp. 80–81.
48. Absorption peak widths do vary among minerals but are always broad [see G. R. Rossman, *Rev. Mineral.* **18**, 207 (1988)], making κ_{rad} low at high temperature. Furthermore, because widths do not change across solid solution series [for example, (*47*)], the radiative conductivity will not be affected by Fe content as long as enough is available to produce at least a small absorption in an appropriate grain size. Thus, minerals with Fe contents below perhaps 1 or 2 weight % should probably be treated as Fe-free.
49. I also tried to fit $\kappa(T)$ by the sum of Eqs. 5a and 9 and obtained approximately the same value for *b*. Those results are not presented because the measurements of κ at high temperature vary among studies (*3, 4, 24*) and are not at sufficiently high temperature to precisely constrain *b*. However, the data (Fig. 1) indicate that *b* is small and that the larger estimates for κ_{rad} (*18, 23*) are inconsistent with total κ.
50. Y. Fei, in *Mineral Physics and Crystallography: A Handbook of Physical Constants*, T. J. Ahrens, Ed. (American Geophysical Union, Washington, DC, 1995), pp. 29–44.
51. K. Horai, *J. Geophys. Res.* **76**, 1278 (1971).
52. C. B. Agee, *Annu. Rev. Earth Planet. Sci.* **21**, 19 (1993).
53. The pressure dependence obtained from Eq. 10 using the data in Table 1 with $q = 0$ [see A. M. Hofmeister, J. Xu, H. K. Mao, P. M. Bell, T. C. Hoering, *Am. Mineral.* **74**, 281 (1989)] gave negligibly different values from Eq. 11. For silicate Pv, *q* is unknown and γ and *K*′ have large uncertainties. Thus, results for Eq. 11 are given.
54. A. M. Hofmeister, unpublished data. Fe end-member spectra are in P. F. McMillan and A. M. Hofmeister, *Rev. Mineral.* **18**, 99 (1988).
55. H. Fujisawa, N. Fujii, H. Mizutani, H. Kanamori, S. Akimoto, *J. Geophys. Res.* **75**, 4727 (1968).
56. M. Manga and R. Jeanloz, *ibid.* **102**, 2999 (1997).
57. H. Yutatake and M. Shimada, *Phys. Earth Planet. Inter.* **17**, 193 (1978).
58. W. R. McPherson and H. H. Schloessin, *ibid.* **29**, 58 (1982).

59. S. Andersson and G. Bäckström, *Rev. Sci. Instrum.* **57**, 1633 (1986).
60. T. Katsura, *Phys. Earth Planet. Inter.* **101**, 73 (1997).
61. M. Osako and E. Ito, *Geophys. Res. Lett.* **18**, 239 (1991).
62. N. L. Ross and R. M. Hazen, *Phys. Chem. Miner.* **16**, 415 (1989).
63. R. Lu, A. M. Hofmeister, Y. Wang, *J. Geophys. Res.* **99**, 11795 (1994).
64. C. A. Stein and S. Stein, *Nature* **359**, 123 (1992); B. Parsons and J. G. Sclater, *J. Geophys. Res.* **82**, 803 (1977).
65. M. L. Renkin and J. G. Sclater, *ibid.* **93**, 2919 (1988); J. G. Sclater and L. Wilson, in *The Geology of North America: The Western North Atlantic*, P. R. Vogt and B. E. Tucholke, Eds. (Geological Society of America, Boulder, CO, 1986), pp. 257–270.
66. This approach is consistent with solutions of steady-state heat flow between stacked parallel planes [see section 3.2 in (*1*)]. It is reasonable because the pressure dependence is weak (κ doubles over 760 km).
67. A. M. Dziewonski and D. L. Anderson, *Phys. Earth Planet. Inter.* **25**, 297 (1981).
68. T. Inoue and H. Sawamoto, in (*7*), pp. 323–331. The 1-atm value is the same as the dry solidus [see A. E. Ringwood, *Composition and Petrology of the Earth's Mantle* (McGraw-Hill, New York, 1975)].
69. J. B. Gaherty, T. H. Jordon, L. S. Gee, *J. Geophys. Res.* **101**, 22291 (1996).
70. Y. Xu and D. A. Weins, *ibid.* **102**, 27439 (1997).
71. E. Takahashi, *ibid.* **91**, 9367 (1986).
72. D. L. Turcotte and G. Schubert, *Geodynamics* (Wiley, New York, 1982).
73. E. Ito and T. Katsura, *Geophys. Res. Lett.* **16**, 425 (1989).
74. E. Ito and E. Takahashi, *J. Geophys. Res.* **94**, 10637 (1989); E. Ito and T. Katsura, in (*7*), pp. 315–322.
75. D. C. Presnall, Y. H. Weng, C. S. Milholland, M. J. Walter, *Phys. Earth Planet. Inter.* **107**, 83 (1998).
76. E. Ohtani, K. Moriwaki, T. Kato, K. Omuma, *ibid.*, p. 75.
77. A. Zerr, A. Diegeler, R. Boehler, *Science* **281**, 243 (1998).
78. T. Katsura and E. Ito, *J. Geophys. Res.* **94**, 15663 (1986).
79. F. D. Stacey, *Phys. Earth Planet. Inter.* **15**, 341 (1977).
80. J. M. Brown and T. J. Shankland, *Geophys. J. R. Astron. Soc.* **66**, 579 (1981).
81. R. Boehler, *Earth Planet. Sci. Lett.* **111**, 217 (1992).
82. ———, *Annu. Rev. Earth Planet. Sci.* **24**, 15 (1996); F. D. Stacey, in preparation.
83. F. D. Stacey and D. E. Loper, *Phys. Earth Planet. Inter.* **33**, 45 (1983).
84. D. L. Anderson, *Theory of the Earth* (Blackwell Scientific, Boston, 1989).
85. J. Verhoogen, *Phys. Earth Planet. Inter.* **7**, 47 (1973); F. D. Stacey, *Physics of the Earth* (Brookfield, Brisbane, Australia, 1992).
86. O. L. Anderson, *Phys. Earth Planet. Inter.* **109**, 179 (1998).
87. S. Zhong and M. Gurnis, *J. Geophys. Res.* **99**, 15683 (1994); B. H. Hager, *Eos* **71**, 1567 (1990).
88. Y. Sumino and O. Anderson, in *Handbook of Physical Properties of Rocks III*, R. S. Carmichael, Ed. (CRC Press, Boca Raton, FL, 1984), pp. 139–280; J. D. Bass, in (*50*), pp. 45–63; E. Knittle, *ibid.*, pp. 98–142.
89. H. Cynn and A. M. Hofmeister, *J. Geophys. Res.* **99**, 17717 (1994).
90. T. Ashida, S. Kume, E. Ito, A. Navrotsky, *Phys. Chem. Miner.* **16**, 239 (1988).
91. A. M. Hofmeister, in (*34*), pp. 215–227.
92. A. E. Beck, D. M. Darba, H. H. Schloessin, *Phys. Earth Planet. Inter.* **17**, 35 (1978).
93. G. H. Scharmli, in *High Pressure Research in Geosciences*, W. Schreyer, Ed. (Schweizerbartsche, Stuttgart, Germany 1982), pp. 349–373.
94. H. H. Schloessin and Z. Dvorak, *Geophys. J. R. Astron. Soc.* **27**, 499 (1972).
95. M. Osako and Y. Kobayashi, *Phys. Earth Planet. Inter.* **18**, P1 (1979).
96. S. W. Kieffer, I. C. Getting, G. C. Kennedy, *J. Geophys. Res.* **81**, 3018 (1976).
97. K. Horai and J. Sasaki, *Phys. Earth Planet. Inter.* **55**, 292 (1989).
98. Å. Franson and R. G. Ross, *J. Phys. C Solid State Phys.* **12**, 219 (1983).
99. I thank R. Boehler for suggesting this problem, the Humboldt Foundation for making our interaction possible, and the David and Lucile Packard Foundation for funding the IR spectroscopy that formed the basis of this study. The input of O. L. Anderson, A. Chopelas, R. E. Criss, R. F. Dymek, S. A. Hauck, R. Phillips, P. Shore, M. Simons, D. Weins, M. Wyssession, and four anonymous reviewers is greatly appreciated. The project was partially supported by NSF grant EAR712311.

25 August 1998; accepted 4 January 1999

A Well-Collimated Quasi-Continuous Atom Laser

E. W. Hagley,[1] L. Deng,[1,2] M. Kozuma,[3] J. Wen,[1] K. Helmerson,[1]
S. L. Rolston,[1] W. D. Phillips[1]

Extraction of sodium atoms from a trapped Bose-Einstein condensate (BEC) by a coherent, stimulated Raman process is demonstrated. Optical Raman pulses drive transitions between trapped and untrapped magnetic sublevels, giving the output-coupled BEC fraction a well-defined momentum. The pulsed output coupling can be run at such a rate that the extracted atomic wave packets strongly overlap, forming a highly directional, quasi-continuous matter wave.

The occupation of a single quantum state by a large number of identical bosons (*1–5*) is a matter-wave analog to the storage of photons in a single mode of a laser cavity. Just as one extracts a coherent, directed beam of photons from a laser cavity by using a partially transmitting mirror as an output coupler, one can analogously extract directed matter waves from a condensate. Such a source of matter waves, or "atom laser," is important in the field of atom optics (*6*), the manipulation of atoms analogous to the manipulation of light. Its development is providing atom sources that are as different from ordinary atomic beams as lasers are from light bulbs.

The first demonstration of a BEC output coupler was reported in 1997 (*7*) where coherent, radiofrequency (rf)-induced transitions were used to change the internal state (magnetic sublevel) of the atoms from a trapped to an untrapped state. This method, however, did not allow the direction of the output-coupled atoms to be chosen. The extracted atoms fell under the influence of gravity and expanded because of their intrinsic repulsion. We demonstrate a highly directional method to optically couple out a variable fraction of a condensate and apply this method to produce a well-collimated, quasi-continuous beam of atoms, an important step toward a truly continuous wave (cw) atom laser (*8*).

The output coupling is based on stimulated Raman transitions between magnetic sublevels (*9, 10*). The sublevel into which the atoms are transferred is unaffected by the trapping potential, and the process imparts a well-defined momentum to the output-coupled condensate fraction. In contrast, previous work on Bragg diffraction (*11*) transferred momentum without changing the internal state of the atom. A single Raman pulse can couple out any desired fraction of the condensate. By changing the angle between the wave vectors $\mathbf{k}$ of the Raman lasers ($k = 2\pi/\lambda$, $\lambda = 589$ nm) and using higher order ($2n$-photon) Raman transitions, it is possible to impart any momentum of magnitude 0 to $2n\hbar k$ (*11*) to the atoms (for sodium, $2\hbar k$ corresponds to a velocity of 6 cm/s). In this way it is possible to choose the energy of the extracted deBroglie wave, producing a widely tunable atom laser.

In this experiment, we used a hybrid evaporation technique with a time orbiting potential (TOP) trap (*12, 13*) to form a sodium condensate (*11*). We typically obtain a condensate, without a discernible normal fraction, with about 10^6 atoms in the $3S_{1/2}$, $F = 1$, $m = -1$ state (*14*). Once the condensate is formed we adiabatically expand the trapping potential in 0.5 s, reducing the trapping frequencies to $\omega_x/2\pi = 18$ Hz, $\omega_y/2\pi = 25$ Hz, and $\omega_z/2\pi = 35$ Hz. We have measured (*15*) that our adiabatic cooling reduces the asymptotic root mean square (rms) momentum width of the released condensate to $0.09(1)\hbar k$ (*16*).

In Raman output coupling (Fig. 1), a moving standing wave, composed of two nearly counterpropagating laser beams with frequency difference $\delta = \omega_2 - \omega_1$ (*17*), is

---

[1] National Institute of Standards and Technology, Gaithersburg, MD 20899, USA. [2] Georgia Southern University, Statesboro, GA 30460, USA. [3] Institute of Physics, University of Tokyo, Tokyo 153-8902, Japan.